Korean J. Chem. Eng., 39(9), 2532-2541 (2022)
DOI: 10.1007/s11814-022-1131-2

pISSN: 0256-1115
eISSN: 1975-7220

Microwave-assisted synthesis of $MgFe_2O_4$-decorated UiO-66(Zr)-NH_2 composites for collaborative adsorption and photocatalytic degradation of tetracycline

The Ky Vo*, Minh Tien Nguyen*, Van Cuong Nguyen*,†, and Jinsoo Kim,†**

*Chemical Engineering Department, Industrial University of Ho Chi Minh City,
12 Nguyen Van Bao, Go Vap, Ho Chi Minh City, Vietnam
**Department of Chemical Engineering (Integrated Engineering), Kyung Hee University,
1732 Deogyeong-daero, Yongin, Gyeonggi-do 17104, Korea
(*Received 23 December 2021 • Revised 11 March 2022 • Accepted 2 April 2022*)

Abstract−$MgFe_2O_4$-decorated UiO-66(Zr)-NH_2 composites (MFO@UN) with different blending ratios were efficiently prepared by microwave-assisted synthesis. The results indicate that the hybrid composite exhibits high surface area and magnetic properties. Moreover, combining ferrite into the UiO-66(Zr)-NH_2 framework produces a heterojunction structure and an interfacial interaction that improves the composite's visible-light absorption. Tetracycline removal experiments show that the MFO@UN composites exhibit excellent photodegradation performance compared with the pure ferrite and MOF. The optimal 1.5MFO@UN catalyst (molar $Zr^{4+}/MgFe_2O_4$=1.5) exhibits the highest removal efficiency of approximately *ca.* ~92% after 90 min of pre-adsorption and 160 min of visible-light illumination. The photocatalytic mechanism investigation reveals that photo-induced holes (h^+) and ·OH radicals predominantly govern the photodegradation process. Notably, the separation and immigration of the photo-induced holes and electrons improve due to the heterojunction structures that form between the two semiconductors. In addition, the prepared catalysts are highly recoverable and renewable. These findings suggest that the microwave-derived $MgFe_2O_4$@UiO-66(Zr)-NH_2 catalyst may be a promising candidate for treating organic contaminants in wastewater.

Keywords: $MgFe_2O_4$, UiO-66(Zr)-NH_2, Microwave, Photocatalyst, Visible-light, Tetracycline

INTRODUCTION

Water pollution caused by antibiotic pollutants is one of society's main issues. Released antibiotic residues and their metabolites retain their biological activity, high hydrophilicity, and biological stability, causing toxicity to aquatic organisms, terrestrial animals, and humans [1,2]. The most dangerous effect of these pollutants in the environment is the development of multi-resistant bacterial strains that can no longer be treated with recently known drugs [3,4]. Thus, physical, chemical, and biological methods have been applied to degrade the antibiotics in wastewater. However, these methods come with multiple side effects. A recent promising strategy is the photoreduction of organic contaminants using semiconductors [5-8]. Multiple materials (e.g., TiO_2, ZnO, or Cu_2O) are widely applied in the photocatalytic degradation of organic pollutants [9-12]. Unfortunately, these conventional semiconductors exhibit limitations due to their low adsorptive properties toward pollutants and their poor responses in the visible-light region [9,13]. Metal-organic frameworks (MOFs) have also received significant attention because of these beneficial properties: high surface area, large pore volume, and designable framework [14,15]. Several MOF structures have been successfully utilized as photocatalysts for the degradation of organic pollutants (i.e., MOF-5, MIL-88(Fe), MIL-53(Fe) [16], MIL-125(Ti) [17], Co-based MOFs [18], and zirconium-based MOFs [19]). This demonstrates the possibility that these MOF structures can be excited under UV-visible-light irradiation. However, the photocatalytic performance of pure MOFs is limited because the separation and immigration of the photo-induced charges on the MOFs are not efficient enough [20,21]. Recently, MOF modification with light-harvesting semiconductor materials has been considered an effective strategy for fabricating MOF-based photocatalysts [9,16,21,22]. For instance, MIL-125(Ti), modified by In_2S_3, exhibited improved photocatalytic degradation efficiency toward tetracycline (TC) antibiotics. Similarly, g-C_3N_4-modified UiO-66(Zr) exhibited high photocatalytic performance toward dyes under visible-light irradiation [23]. The prepared Ag_3PO_4/GO/UiO-66-NH_2 showed enhanced visible-light-driven photocatalytic activity compared with a pristine MOF [24]. In addition, MIL-100(Fe) embedded with Ag_3PO_4 exhibited more remarkable photocatalytic ability than pure MIL-100(Fe) [25]. These results indicate that combining an MOF with a particular semiconductor is promising for producing a highly efficient photocatalyst.

The regeneration and recycling of catalysts are crucial in diminishing the impact of the disposal of polluted adsorbents on the environment. However, most photocatalysts are nanoparticles that are not quickly recovered after use. Therefore, the development of recoverable photocatalysts has recently attracted much attention [26,27]. Magnetic materials are promising candidates for industrial application because they can be efficiently recovered using an external field. Magnesium ferrite ($MgFe_2O_4$), one of the representative magnetic

†To whom correspondence should be addressed.
E-mail: nvc@iuh.edu.vn, jkim21@khu.ac.kr

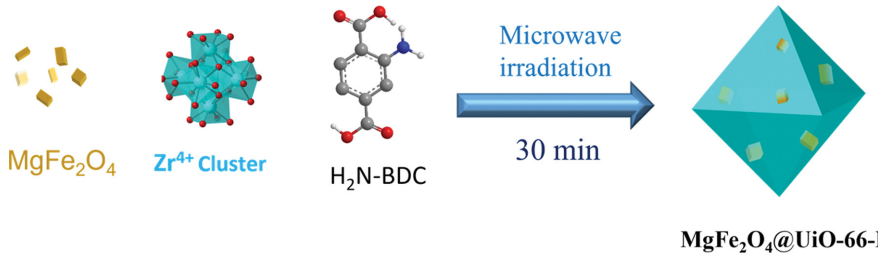

Scheme 1. The schematic diagram for the synthesis of the $MgFe_2O_4$@UiO-66(Zr)-NH_2 composite.

materials, is widely used for wastewater treatment because of its chemical stability, good response toward visible light, and convenient synthesis procedure [28-30]. However, the photocatalytic performance of $MgFe_2O_4$ is low due to the quick recombination that occurs between the photo-induced electrons and holes [31-33]. In addition, $MgFe_2O_4$ has low porosity, inhibiting the accumulation of contaminants.

In this work, UiO-66(Zr)-NH_2 frameworks, decorated with $MgFe_2O_4$, were rapidly and efficiently prepared using the microwave-assisted solvothermal synthesis method (shown in Scheme 1). Different hybrid UiO-66(Zr)-NH_2@$MgFe_2O_4$ composites were obtained by adjusting the MOF/$MgFe_2O_4$ mass ratio. The structural and photoelectrochemical characteristics of the prepared materials were explored by XRD, FT-IR, SEM, TEM, N_2 adsorption, VSM, UV-vis DRS and PL methods. The photocatalytic performance of the UiO-66(Zr)-NH_2@$MgFe_2O_4$ composites was evaluated by removing the TC antibiotics under visible-light illumination. In addition, the photodegradation mechanism was elucidated using radical scavenging experiments. This study's results indicate that the $MgFe_2O_4$-decorated UiO-66(Zr)-NH_2 hybrid composite exhibit lower band-gap energy and more efficient charge transfer energy than the pristine MOF. The results of this study suggest that the microwave-derived $MgFe_2O_4$@UiO-66(Zr)-NH_2 catalyst may be a promising candidate for treating organic contaminants in wastewater.

EXPERIMENTAL

1. Synthesis of $MgFe_2O_4$ Nanoparticles

Nanoparticles of $MgFe_2O_4$ were fabricated following the procedure from the authors' previous work [31]. Briefly, 2.5 mmol $Mg(NO_3)_2 \cdot 6H_2O$ (98%, Sigma-Aldrich) and 5.0 mmol of $Fe(NO_3)_3 \cdot 9H_2O$ (99%, Sigma-Aldrich) were dissolved in deionized water to obtain a solution. Subsequently, citric acid (23 mmol) was added and stirred for 6 h to produce a thick gel. The resultant gel was then calcined at 650 °C for 7 h to yield the $MgFe_2O_4$ nanoparticles.

2. Microwave-assisted Synthesis of $MgFe_2O_4$@UiO-66(Zr)-NH_2

The $MgFe_2O_4$ nanoparticles were dispersed in 50 mL dimethylformamide (DMF) and sonicated in a 200 mL beaker. To the solution, 1.72 mmol $ZrCl_4$ (99.8%, Sigma-Aldrich), 1.72 mmol 2-amino terephthalic acid (2-amino-1,4-benzenedicarboxylic acid; 99%, Sigma-Aldrich), and acetic acid were added. Afterward, the mixture was transferred into a Teflon autoclave and heated in a microwave oven (ETHOS One, MLS) for 30 min. The microwave irradiation power was kept at a constant value of 350 W (2.5 GHz) to obtain the desired temperature of 120 °C. After the reaction occurred, the solution was centrifuged and the resulting solid product was collected. The solid product was then washed with N,N-dimethylformamide (DMF, 99%) and ethanol (EtOH, 99%) at 70 °C for 6 h. Finally, the product was dried in ambient air at 120 °C for 12 h. The prepared samples were denoted as *m*MFO@UN [the term *m* indicates the molar ratio of $ZrCl_4/MgFe_2O_4$ (*m*=0.5, 1.5, and 2.5)]. Pristine UiO-66(Zr)-NH_2 was synthesized utilizing the above procedure without the addition of ferrite. All samples were heated and vacuumed at 120 °C for 8 h before use.

3. Characterization

The crystallographic structure of the prepared amino-functionalized UiO-66(Zr), $MgFe_2O_4$, and MFO@UN composites was examined with an XRD analyzer (MAC-18XHF, Rigaku, Japan) under Cu-Kα radiation (λ=1.54 Å). A field emission scanning electron microscope (Leo-Supra 55, Carl Zeiss S.T.M., Germany) was utilized to obtain the morphology of the samples. The N_2 adsorption at 77 K was analyzed utilizing a Micromeritics instrument (BELSORP-max, BEL, Japan). The specific surface area was obtained via the multiple point Brunauer-Emmett-Teller (BET) method in the pressure range of $0.05<P/P_0<0.1$. The pore size distributions were analyzed using the Horvath-Kawazoe (HK) method. The functional groups of the catalysts were detected via FTIR spectroscopy (FTIR 4700, JASCO, Japan) at the Core Facility Center for Analysis of Optoelectronic Materials and Devices of the Korea Basic Science Institute (KBSI). The materials' thermal stability was analyzed by thermogravimetric analysis (TGA; Q50, TA Instruments, USA) under air condition at a heating rate of 10 °C min^{-1}. The UV-vis absorbance spectra were obtained through a spectrophotometer (Lambda 950 UV-vis-NIR, Perkin Elmer, USA). The magnetic measurements at ambient temperature were analyzed with a vibrating sample magnetometer (VSM; JDM-13, China). Finally, the fabricated materials' PL spectra were obtained with an FL920 fluorescence spectrometer (Edinburgh Instruments Ltd.) that was equipped with a 450 W xenon (Xe) lamp. Total organic carbon (TOC) was measured by the Shimadzu TOC-VCPH analyzer.

4. Photocatalytic Degradation Tests

The photodegradation of the tetracycline antibiotics ($C_{22}H_{24}N_2O_8$, Sigma-Aldrich, 99%) was carried out using a photochemical reaction cell installed with a 500 W Xe lamp and an optical filter (λ> 420 nm). The weighed catalyst (80-280 mg/L) was dispersed in 50 ml of TC solution (15-70 mg/L) and stirred in the dark for 90 min. Afterward, the reaction mixture was continuously stirred and exposed to visible light. The content of the antibiotic in the solution was measured using a UV-vis spectrophotometer (Optizen P.O.P., Mecasys, Korea) at the λ_{max}=357 nm.

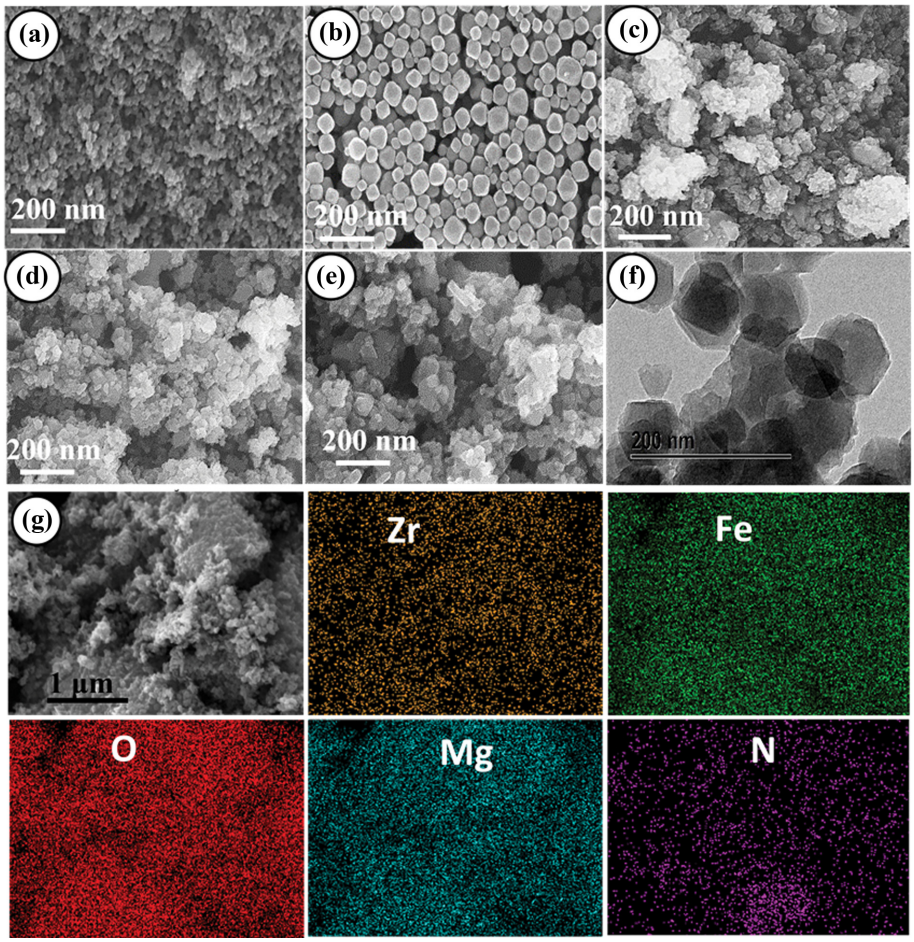

Fig. 1. SEM images of (a) $MgFe_2O_4$, (b) UiO-66(Zr)-NH_2, (c) 0.5MFO@UN, (d) 1.5MFO@UN, (e) 2.5MFO@UN, and (f) TEM image of 1.5MFO@UN; (g) EDX mapping of Zr, Fe, O, Mg and N on the 1.5MFO@UN sample.

RESULTS AND DISCUSSION

1. Characterization

The morphology analyses of the samples are illustrated in Fig. 1. The SEM image of $MgFe_2O_4$ shows aggregated spheroidal-shaped nanoparticles with a diameter ranging from approximately 20-50 nm [Fig. 1(a)]. The SEM image of pristine UiO-66(Zr)-NH_2 shows octahedral particles with a particle size in the approximate range of 30-100 nm [Fig. 1(b)]. Figs. 1(c)-(e) demonstrate that the microwave-derived MFO@UN composites are highly aggregated particles; this suggests that the ferrite nanoparticles provide a platform for the continuous secondary nucleation of the MOF under microwave illumination. The TEM images reveal the well-developed heterogeneous structure of the MFO@UN composites [Fig. 1(f)]. In addition, the SEM energy dispersive X-ray spectroscopy analyses show that the Mg, Fe, O, N, and Zr elements were dispersed throughout the samples [Fig. 1(g)].

The crystalline structure of the prepared materials was characterized by XRD analysis, and the results are presented in Fig. 2(a). The XRD pattern of the $MgFe_2O_4$ shows the diffraction peaks at 2θ=30.21°, 35.57°, 43.35°, 57.18°, and 62.72°, all of which were assigned to the spinel structure of $MgFe_2O_4$ [7,34]. The XRD analysis indicates that the resulting UiO-66(Zr)-NH_2 structure was a typical UiO-66(Zr) framework. As shown in Fig. 2(a), the ferrite's characterized peaks were slightly shifted on the composites' XRD patterns. In addition, the XRD patterns of the hybrid MFO@UN composites exhibit reduced peak intensity compared with the pristine samples, suggesting that the $MgFe_2O_4$ nanoparticles were successfully incorporated into the MOF framework. FTIR analyses were performed to reveal the functional groups of the prepared materials, as is presented in Fig. 2(b). For UiO-66(Zr)-NH_2, the spectrum shows a double peak around 3,360-3,485 cm^{-1} that is attributed to the vibration of the NH_2 (an amino group). In addition, the bending of the N-H bond (1,624 and 1,586 cm^{-1}) [35] and the stretching of the C-N bond (1,256 and 1,338 cm^{-1}) of the aromatic amines [35,36] were observed. The Zr-O bond formed between the Zr^{4+} and the carboxylate ligand was characterized by the low wavenumber peak at approximately 640 cm^{-1}. Aspresented in Fig. 2(b), the FTIR spectrum of the $MgFe_2O_4$ shows two vibrational modes (568 and 440 cm^{-1}); these modes were assigned to the M_{tetra}-O bridge and the M_{octa}-O bridge, respectively [34]. These peaks appear on the FTIR spectra of the composite samples with a considerable decrease in their intensity. Furthermore, the resulting composites have similar scopes to the parent MOF but with reduced

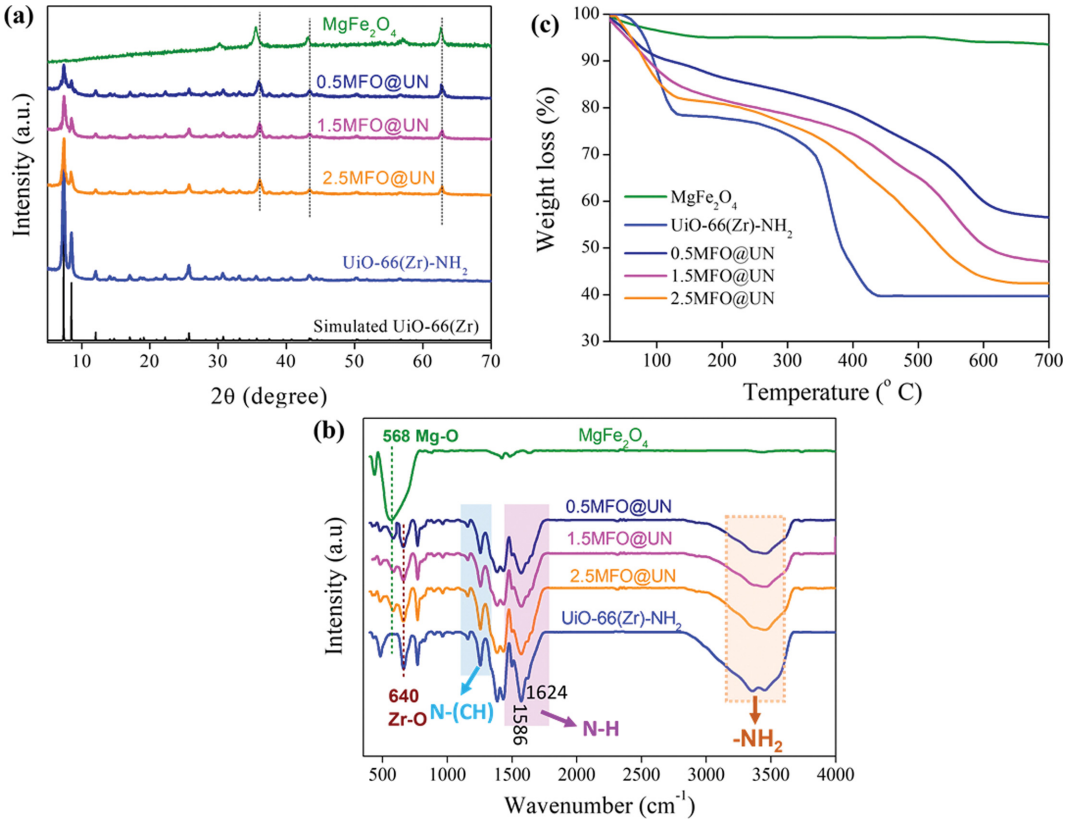

Fig. 2. (a) XRD patterns, (b) FTIR spectra, and (c) TGAs of the prepared samples.

peak intensity, confirming that the hybrid composite was successfully prepared without changing the structure of the pristine materials. TGA analyses were performed for all samples and are shown in Fig. 2(c). $MgFe_2O_4$ demonstrates high thermal stability under the investigated temperature. The TGA curve of the UiO-66(Zr)-NH_2 composite exhibits three weight loss steps, including the evaporation of the solvents (<120 °C), the removal of the solvents inside the pores (120-300 °C), and the decomposition of the MOF ligand (>300 °C). As demonstrated in Fig. 2(c), the UiO-66(Zr)-NH_2 decorated with $MgFe_2O_4$ exhibits improved thermal stability compared with the parent UiO-66(Zr)-NH_2; this is due to the incorporation of the $MgFe_2O_4$.

Figs. 3(a)-(e) show the X-ray photoelectron spectroscopy (XPS) analyses of the prepared $MgFe_2O_4$ and the $MgFe_2O_4$@UiO-66(Zr)-NH_2 composite. The survey scan result proved the existence of Zr, O, C, N, Mg, and Fe in the composite material [Fig. 3(a)]. The Mg 1s core-level XPS spectrum shows one peak at 1,300 eV, attributed to the Mg^{2+} [Fig. 3(b)]. The Fe 2p core-level XPS spectrum shows two binding energy peaks at 710.3 eV (Fe $2p_{3/2}$) and 725 eV (Fe $2p_{1/2}$), assigned to Fe^{2+} in both the $MgFe_2O_4$ and composite samples [15] [Fig. 3(c)]. The high-resolution spectrum of O 1s, showing a binding peak at ~531 eV, is attributed to the O in the Zr-O bond of the MOF [37]; meanwhile, a lower binding energy peak located at ~529.5 eV is ascribed to the O of the Fe-O bond in the $MgFe_2O_4$ [38] [Fig. 3(d)]. The carbon 1s core-level XPS spectrum of the pure MOF and the composite reveals the existence of carbon in the C-C (~285.5 eV) and O-C=O (~288.7 eV) bonds of the terephthalic acid [39,40] [Fig. 3(e)]. Note that incorporating $MgFe_2O_4$ into the amino-functionalized UiO-66(Zr) resulted in slight shifts of these peaks compared with the host. This could be attributed to the electrostatic interaction between the $MgFe_2O_4$ and the BDC ligand of the UiO-66(Zr)-NH_2.

The textural properties of the prepared catalysts were analyzed through N_2 adsorption and pore size distribution, as described in Figs. 4(a)-(b). The UiO-66(Zr)-NH_2 shows high N_2 uptake capacity because of its high surface area and large pore volume. In contrast, the bare $MgFe_2O_4$ exhibits a modest N_2 uptake capacity, suggesting low porosity. As shown, the incorporation of ferrite into the framework of UiO-66(Zr)-NH_2 significantly decreased the N_2 uptake. In addition, the pore size distribution reveals that the pore volume of the composites decreased with an increase in the $MgFe_2O_4$ load. Table 1 lists the calculated BET surface area and pore volume of the fabricated materials, revealing that the porosity of the composites increased as the Zr^{4+}/ferrite molar ratio increased.

Table 1. Textural properties of the prepared samples

Sample	BET, m^2/g	Total pore volume, cm^3/g
$MgFe_2O_4$	38	0.08
0.5MFO@UN	169	0.35
1.5MFO@UN	426	0.42
2.5MFO@UN	856	0.54
UiO-66(Zr)-NH_2	1020	0.71

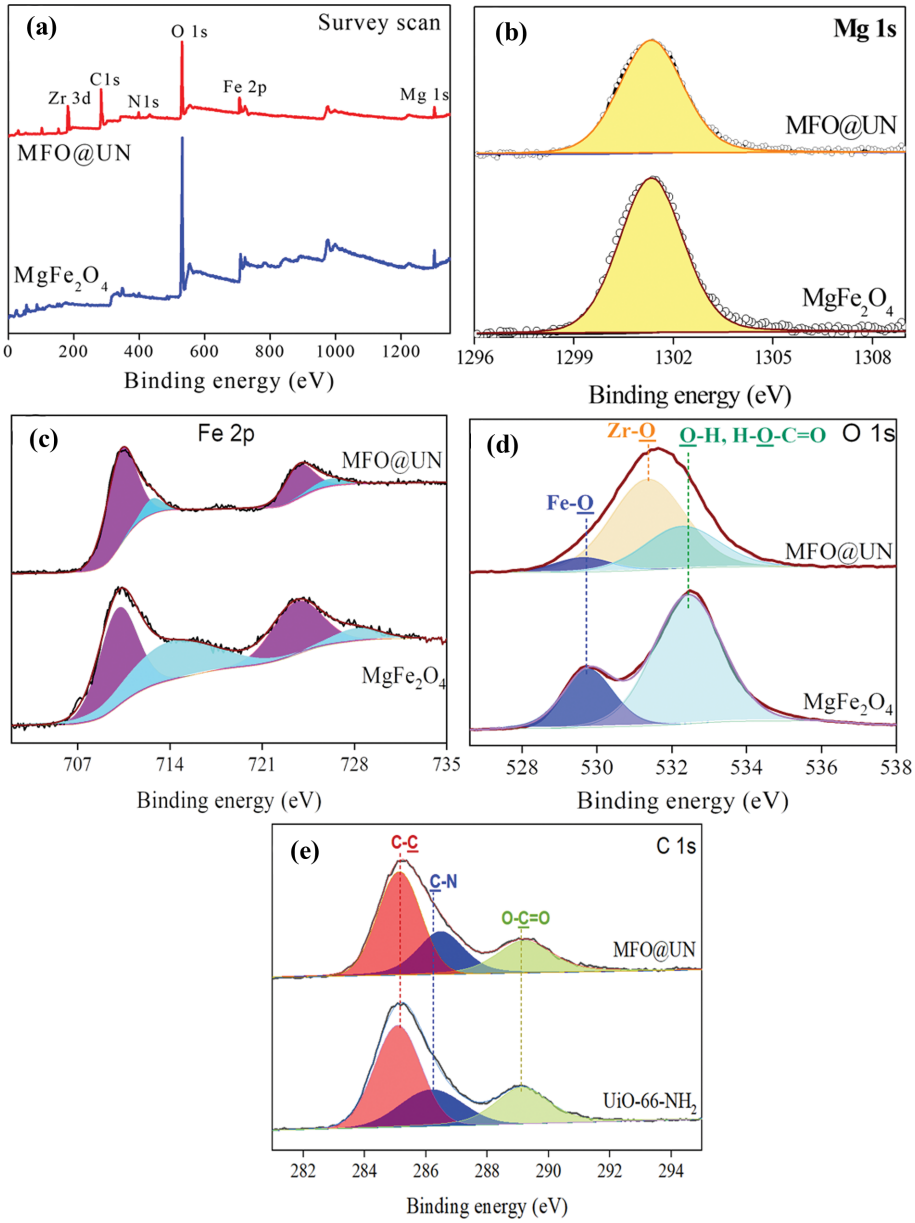

Fig. 3. X-ray photoelectron spectroscopy analyses of the prepared samples: (a) Survey scan, and high-resolution XPS spectrum of (b) Mg 1s, (c) Fe 2P, (d) O 1s, and (e) C 1s.

The magnetic properties of the prepared samples were analyzed through the VSM spectrum, as shown in Fig. 5(a). The bare ferrite $MgFe_2O_4$ shows a saturation magnetization value (M_s) of approximately 61 emu/g, while the M_s values of 0.5MFO@UN, 1.5MFO@UN, and 2.5MFO@UN are approximately 45, 19, and 9 emu/g, respectively. The mass percentage of MOF in 0.5MFO@UN, 1.5MFO@UN, and 2.5MFO@UN (derived from the M_s values) was approximately 26%, 69%, and 85%, respectively. This indicates that the ferrite's magnetic saturation was lowered by loading the amino-functionalized UiO-66(Zr). However, there are insignificant changes in the coercivity values (Hc) of the hybrid composites compared with those in the bare ferrite [the inset of Fig. 5(a)], implying that the ferrite structure was not damaged during the composite synthesis. The magnetic property of the resulting composite was tested with an external magnet [Fig. 5(b)], and the results indicate that the ferrite-decorated UiO-66(Zr)-NH_2 composite was efficiently isolated from the aqueous media. Fig. 5(c) shows the UV-vis DRS of UiO-66(Zr)-NH_2, $MgFe_2O_4$, and the MFO@UN composites. The pure $MgFe_2O_4$ has an absorption edge at approximately 560 nm. The UiO-66(Zr)-NH_2 displays an absorption edge at approximately 475 nm that was induced by a charge transfer from O to Zr in the $Zr_6O_4(OH)_4$ clusters and the influence of the NH_2-BDC ligand. All samples respond well to the visible-light region as they all have absorption edges in the 400-700 nm range. Fig. 5(d) presents the corresponding Tau's plot for the prepared samples. Accordingly, the estimated bandgap energy of $MgFe_2O_4$ and UiO-66(Zr)-NH_2 was about 2.20 and 2.82 eV, respectively. Notably, the bandgap value of 0.5MFO@UN, 1.5MFO@UN, and 2.5MFO@UN

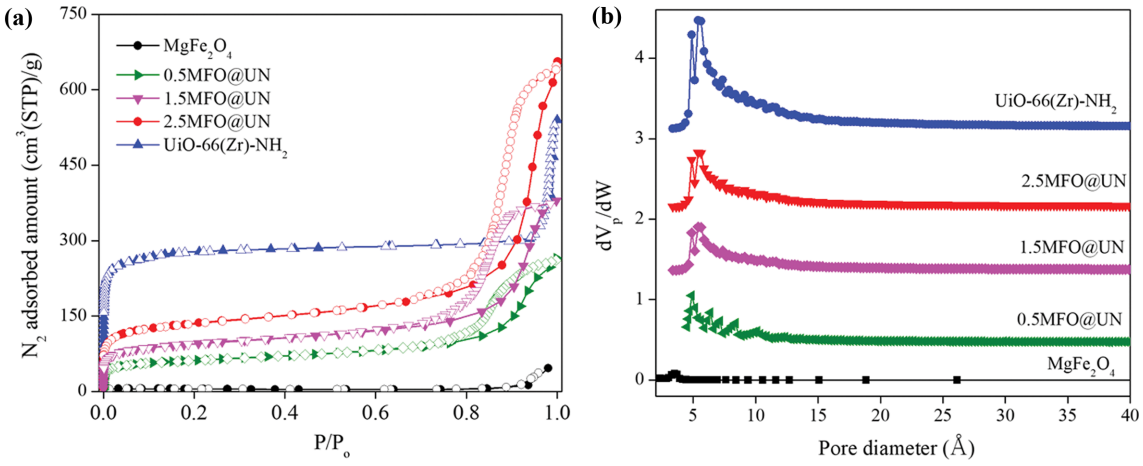

Fig. 4. Textural properties of the samples: (a) N_2 adsorption-desorption isotherms and (b) pore size distributions.

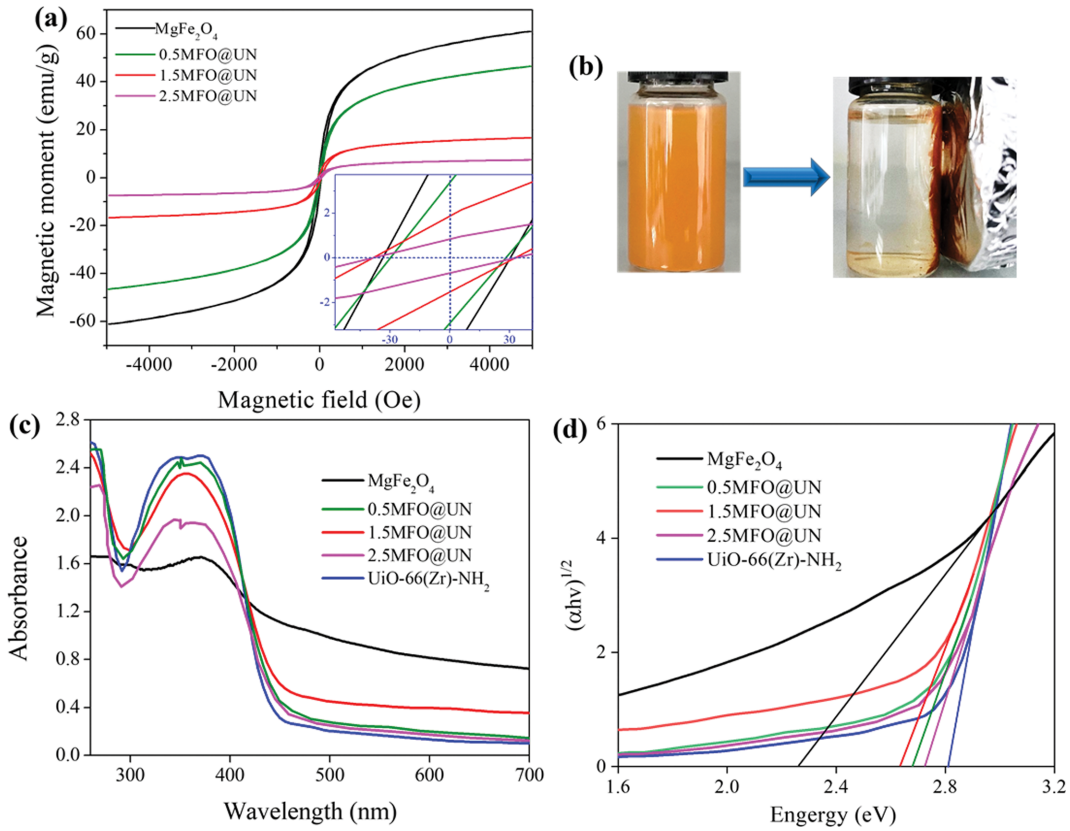

Fig. 5. (a) VSM curve and (b) the recovery of the catalyst by an external magnet; (c) UV-vis DRS and (d) Tau's plot of the synthesized catalysts.

was approximately 2.68, 2.60, and 2.73 eV, respectively. This is lower than the bandgap energy of the parent MOF. This result indicates that the $MgFe_2O_4$-decorated UiO-66(Zr)-NH_2 material is not a physical mixture of ferrite and MOF; instead, its structure is formed from interfacial interactions and heterojunction structures.

The PL analyses provided information about the recombination of the photo-induced electron-hole pairs of the photocatalyst. As demonstrated in Fig. 6, the amino-functionalized UiO-66 MOF has a strong emission peak at approximately 450 nm, similar to the previous reports [19,21]. However, remarkably, the PL intensities were substantially reduced as $MgFe_2O_4$ was introduced, providing evidence of a favorable charge transfer within the composite.

2. Removal of Antibiotics

Figs. 7 (a)-(b) show the TC removal efficiency over the prepared $MgFe_2O_4$, UiO-66(Zr)-NH_2, and ferrite-decorated UiO-66(Zr)-NH_2 composites after 90 min of pre-adsorption in the dark and 160 min of visible-light illumination. The sole $MgFe_2O_4$ ferrite shows a meager removal yield of TC; this could be caused by the fact that the ferrite has a low surface area and low pore volume. For the pristine UiO-66(Zr)-NH_2, the removal efficiency of TC was predomi-

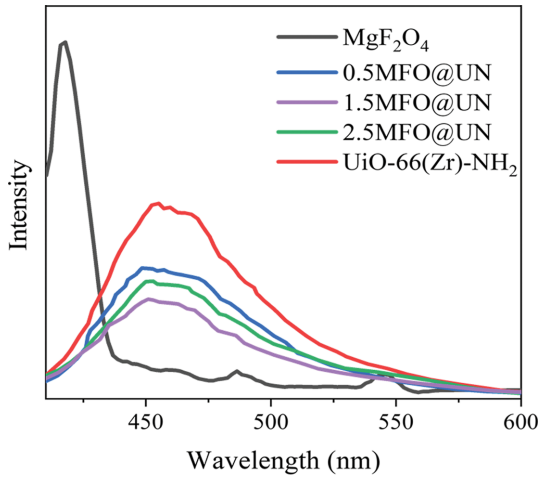

Fig. 6. PL spectra of the synthesized catalysts.

nantly driven by the adsorption process (about 53%); meanwhile, the photolytic degradation of TC was negligible. This is because the amino-functionalized UiO-66(Zr) is highly porous with abundant -NH_2 groups, so it favors the capture of the antibiotic molecules. However, the charge transfer between the ligand and the Zr-O oxo-clusters of the framework is not efficient, which inhibits its photocatalytic performance [22,41]. Compared with the bare $MgFe_2O_4$ ferrite, the adsorption ability of the MFO@UN composites in the pre-adsorption stage was considerably improved [Fig. 7(b)]. Remarkably, the photocatalytic activity of the hybrid UNH@MFO composites was significantly enhanced compared with the parent materials. After 160 min of exposure to visible light, the removal yield of TC onto the fabricated 0.5MFO@UN, 1.5MFO@UN, and 2.5MFO@UN was approximately 39%, 55%, and 43%, respectively; the corresponding total removal yield of TC was approximately 64%, 92%, and 81%, respectively. This improvement in photocatalytic efficiency could be due to the synergic effect that occurs when $MgFe_2O_4$ and UiO-66(Zr)-NH_2 are combined; this effect enhances the photo-induced charge transfer via the interfaces of the semiconductors. Indeed, the photocatalytic efficiency on a mechanical mixer (MIXTURE) containing ferrite and UiO-66(Zr)-NH_2 (approximately Zr^{4+}/ferrite molar ratio=1.5) was much lower than that of the hybrid composite. The combination of UiO-66(Zr)-NH_2 and ferrite enhanced the interfacial charge transfer efficiency and increased the accumulation of TC onto the catalyst's surface; this is when the TC underwent photocatalytic degradation. Note that the high loading content of $MgFe_2O_4$ (Zr^{4+}/$MgFe_2O_4$=0.5) decreased the composite's photocatalytic activity, likely due to the decrease in their porosity (as mentioned above). Fig. 7(c) shows the pseudo-first-order kinetic model and the corresponding degradation rate (k) derived from the photocatalytic kinetic curve of the prepared catalysts. Accordingly, the k for the prepared samples follows this

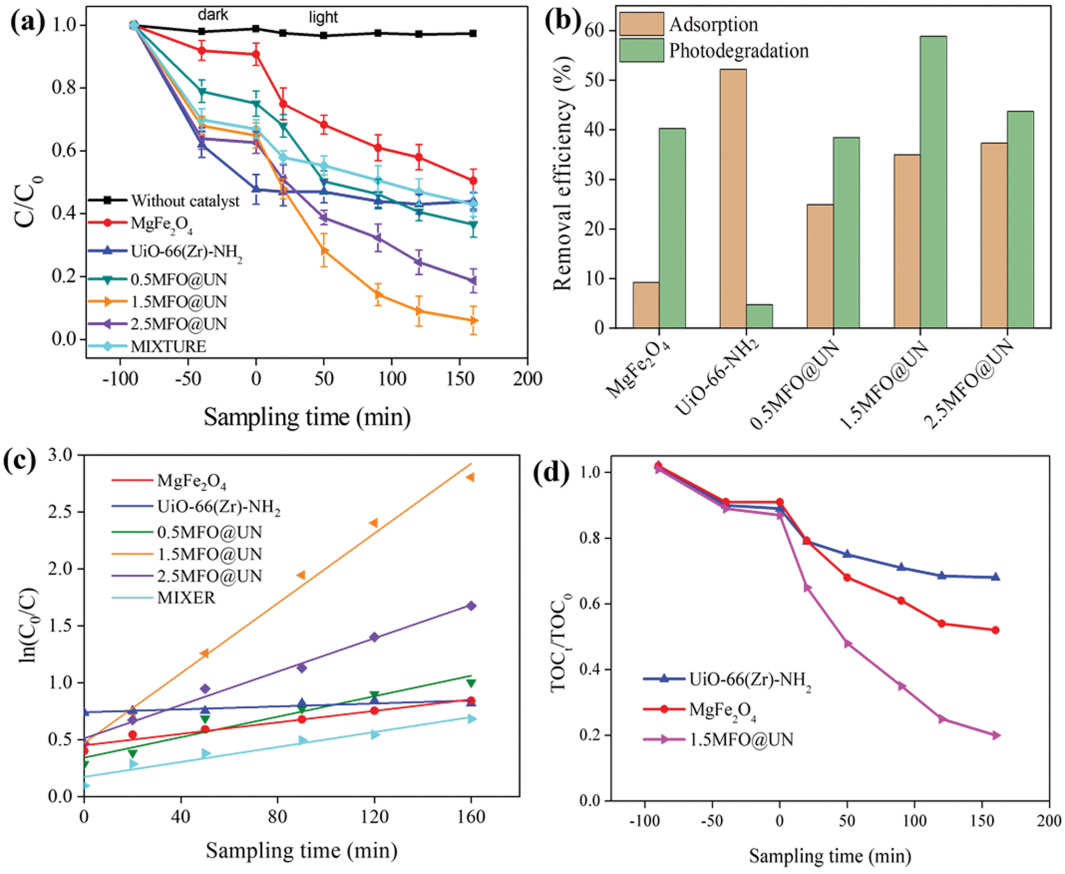

Fig. 7. (a) Adsorption-photocatalytic degradation of TC, (b) TC removal efficiency, (c) pseudo-first-order kinetic model for the photodegradation of TC, and (d) TOC removal efficiency.

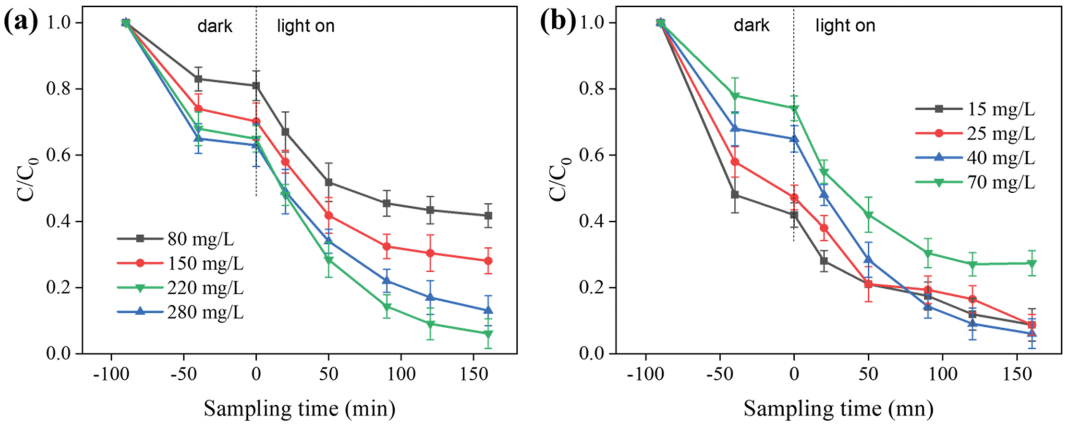

Fig. 8. Effects of (a) catalytic dosage and (b) initial concentration of TC on the TC removal efficiency.

order: 1.5MFO@UN (0.0153 min^{-1})>2.5MFO@UN (0.0073 min^{-1})>0.5MFO@UN (0.0045 min^{-1})>$MgFe_2O_4$ (0.0033 min^{-1})>MIXTURE (0.0025 min^{-1})>UiO-66(Zr)-NH_2 (0.0006 min^{-1}). The hybrid composite 1.5MFO@UN had the maximum photodegradation rate of 0.0153 min^{-1}, which is ~4.6 times higher than the rate of the $MgFe_2O_4$ and ~26 times higher than the rate of the UiO-66(Zr)-NH_2. The higher photocatalytic performance of the $MgFe_2O_4$-decorated UiO-66-NH_2 catalysts suggests that a synergic effect occurs when combining two types of semiconductors into a composite structure; this effect would enhance the separation and immigration of the photogenerated species. In addition, the results reveal that the maximum photocatalytic efficiency was achieved at a particular MOF/ferrite ratio of the composite; at this ratio, the interfacial charge transfer within the heterogeneous structure was optimized. To further certify the photocatalytic degradation of tetracycline antibiotics and the elimination of subsequent organic pollutants, the total organic carbon (TOC) removal was performed to assess the mineralization ability. As shown in Fig. 7(d), the optimal 1.5MFO@UN catalyst shows the highest TOC removal efficiency within 160 min irradiation, reaching approximately 69%; meanwhile, the TOC removal efficiency over the bare UiO-66(Zr)-NH_2 and $MgFe_2O_4$ was approximately 19% and 40%, respectively. The results indicate the high mineralization potential of tetracycline antibiotics over the microwave-derived $MgFe_2O_4$@UiO-66(Zr)-NH_2 photocatalyst.

The effects of the catalyst loading and the initial concentration of the antibiotic solution on the photodegradation performance are shown in Figs. 8((a) and (b)). As shown in Fig. 8(a), increasing the catalyst dosage from 80 to 220 mg/L increases the contaminant's removal efficiency. However, a higher catalyst amount (260 mg/L) diminishes the photocatalytic efficiency; this was caused by the shielding effect of the light irradiation or by the self-consumption of the generated radicals by the excess catalyst [31,42]. In addition, the experiments were performed with various initial concentrations of TC, as demonstrated in Fig. 8(b). The results indicate that the removal efficiency decreased as the concentration of antibiotics increased, possibly because a large amount of contaminant in the solution may block the pores of the catalyst.

3. Renewability Experiment

Renewability is an essential factor that determines a catalyst's possibility of being used on an industrial scale. This study performed a renewability experiment on the optimal 1.5MFO@UN sample. After use, the catalyst was recovered with an external magnet and submerged in deionized water for 6 h. It was then heated at 115 °C under vacuum conditions for 4 h. The obtained catalyst was then utilized as a regenerated sample. As illustrated in Fig. 9(a), the total

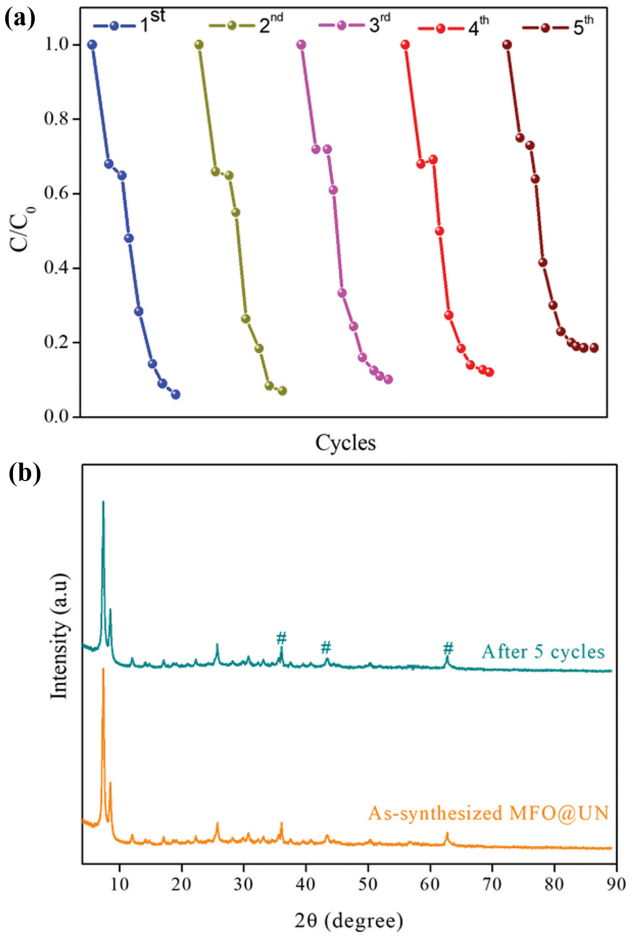

Fig. 9. (a) Recycled degradation efficiency of 1.5MFO@UN and (b) XRD patterns of the catalyst before and after five cycles.

removal efficiency of the contaminant remained nearly the same after the first three cycles. After five cycles (190 min), the removal yield was approximately 80%, suggesting that some of the catalyst's active sites were blocked or deactivated by intermediates after several uses. Fig. 9(b) shows the used catalyst's XRD pattern, demonstrating that the microwave-derived $MgFe_2O_4$@UiO-66(Zr)-NH_2 catalyst was stable after several cycles.

4. Photocatalytic Mechanism

It is well known that photocatalytic degradation is always driven by photo-induced species such as $\cdot O_2^-$, ·OH, and h^+. Benzoquinone (BQ), isopropyl alcohol (IPA), and triethanolamine (TEOA) were used to trap these active radicals produced during the reaction. Reportedly, BQ, IPA, and TEOA are scavengers toward $\cdot O_2^-$, ·OH, and h^+, respectively. As depicted in Fig. 10(a), when BQ was added, there was an insignificant change in the photocatalytic degradation of TC. Conversely, when IPA or TEOA were added to the reaction mixture, the removal efficiency of TC was remarkably inhibited. These results reveal that the photo-induced h^+ and ·OH species predominantly govern the photodegradation process. As the prepared hybrid MFO@UN composite responded in the visible-light region, the electrons and holes were generated during the irradiation process. The photo-induced species reacted with the adsorbed water to generate ·OH radicals when the redox potential

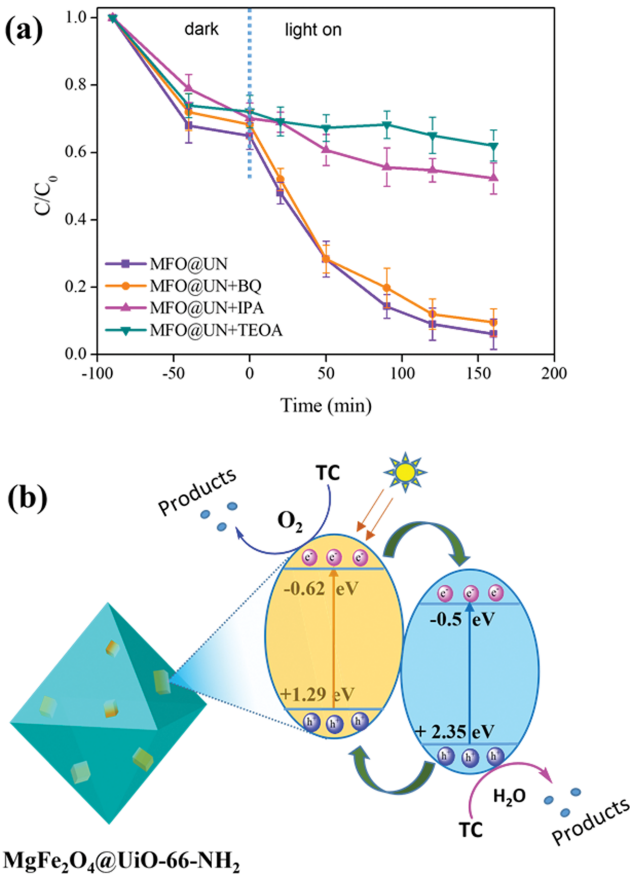

Fig. 10. (a) Removal of TC in the presence of different radical scavengers and (b) the proposed possible reaction mechanism for the photodegradation of TC over the $MgFe_2O_4$@UiO-66(Zr) composite.

conditions were satisfied. The conduction bands (CBs) of $MgFe_2O_4$ and amino-functionalized UiO-66(Zr) were approximately −0.62 V versus NHE [43,44] and −0.5 V versus NHE [9,21], respectively. By combining these results with the bandgap values derived from the UV-vis DRS analyses, the VB values of $MgFe_2O_4$ and UiO-66(Zr)-NH_2 were +1.29 V versus NHE and +2.35 V versus NHE, respectively. As the VB of UiO-66(Zr)-NH_2 is higher than the potential energy of H_2O/·OH (+2.27 V versus NHE), the photogenerated h^+ radicals of an MOF can oxidize the adsorbed H_2O molecules to yield highly reactive ·OH radicals. In addition, the CB potentials of both $MgFe_2O_4$ and UiO-66(Zr)-NH_2 are more negative than the standard potential of $O_2/\cdot O_2^-$ (−0.33 V versus NHE) and O_2/HOO· (−0.037 V versus NHE) [45]. Therefore, the electrons in the CB position of $MgFe_2O_4$ and MOF can reduce O_2 to give $\cdot O_2^-$ or HOO·, followed by the generation of ·OH radicals. Note that the CB potential of $MgFe_2O_4$ is more negative than that of UiO-66(Zr)-NH_2. Consequently, the electrons generated in the CB position of $MgFe_2O_4$ can immigrate to the CB position of the UiO-66(Zr)-NH_2 framework. Meanwhile, the photoexcited holes from the VB position of UiO-66(Zr)-NH_2 immigrated to the less positive VB position of $MgFe_2O_4$. The transfer of the photogenerated species via the composite interfaces may prohibit recombination, and this greatly enhances the photocatalytic efficiency. The above analyses describe a possible mechanism for the photodegradation of tetracycline antibiotics over the microwave-derived $MgFe_2O_4$@UiO-66(Zr)-NH_2 catalyst, shown in Fig. 10(b).

CONCLUSIONS

Hybrid $MgFe_2O_4$@UiO-66(Zr)-NH_2 composites were rapidly prepared by the microwave-assisted solvothermal method. Combining the nanoparticles of the ferrite and UiO-66(Zr)-NH_2 frameworks resulted in a synergic effect, producing heterogeneous structures with a high surface area and low bandgap value. As the Zr^{4+}/ferrite molar ratio increased from 0.5 to 1.5 to 2.5, the surface area of the prepared catalysts increased from 169 to 426 to 856 m^2/g, respectively. Additionally, the bandgap values were approximately 2.68, 2.60, and 2.73 eV, respectively, all of which were lower than the pristine UiO-66(Zr)-NH_2 bandgap value (approximately 2.82 eV). The analyses revealed enhanced photo-induced species transfer and suggested that heterojunction structures had formed between the two semiconductors. As a result, the composite MFO@UN showed improved photocatalytic activity toward tetracycline antibiotics under visible-light irradiation. The optimal composite MFO@UN achieved a high TC removal efficiency (approximately 92%) that was significantly greater than the removal efficiencies of $MgFe_2O_4$ (approximately 48%) and UiO-66(Zr)-NH_2 (approximately 57%). The photocatalytic reaction mechanism was primarily controlled by the h^+ and ·OH radicals. Furthermore, the microwave-derived $MgFe_2O_4$@UiO-66(Zr)-NH_2 composite was highly recoverable and renewable, making it a promising photocatalyst for wastewater treatment.

ACKNOWLEDGEMENT

This work was supported by the Industrial University of Ho Chi Minh City, Vietnam (21.2CNHH02).

FUNDING

This work was supported by the Industrial University of Ho Chi Minh City, Vietnam (21.2CNHH02).

CONFLICT INTEREST

The authors declare that they have no conflict of interest.

REFERENCES

1. S. Wu, H. Hu, Y. Lin, J. Zhang and Y. H. Hu, *J. Chem. Eng.*, **382**, 122842 (2020).
2. T. K. Vo and J. Kim, *Environ. Sci. Pollut. Res.*, **28**, 68261 (2021).
3. X.-D. Zhu, Y.-J. Wang, R.-J. Sun and D.-M. Zhou, *Chemosphere*, **92**, 925 (2013).
4. M. Addamo, V. Augugliaro, A. D. Paola, E. García-López, V. Loddo, G. Marcì and L. Palmisano, *J. Appl. Electrochem.*, **35**, 765 (2005).
5. T. R. Gurugubelli, B. Babu, J. Kim and K. Yoo, *Chem. Pap.*, **75**, 6407 (2021).
6. Z. Man, Y. Meng, X. Lin, X. Dai, L. Wang and D. Liu, *J. Chem. Eng.*, **431**, 133952 (2022).
7. K. D. McDonald and B. M. Bartlett, *Inorg. Chem.*, **60**, 8704 (2021).
8. Y. Ran, J. Zhong, J. Li, M. Li and C. Tian, *Environ. Technol.*, In press (2022).
9. Q. Du, P. Wu, Y. Sun, J. Zhang and H. He, *J. Chem. Eng.*, **390**, 124614 (2020).
10. V.-H. Nguyen, T.-T. Thi Vo, H. Huu Do, V. Thuan Le, T. D. Nguyen, T. Ky Vo, B.-S. Nguyen, T. T. Nguyen, T. K. Phung and V. A. Tran, *Chem. Eng. Sci.*, **232**, 116381 (2021).
11. R. A. Palominos, M. A. Mondaca, A. Giraldo, G. Peñuela, M. Pérez-Moya and H. D. Mansilla, *Catal. Today*, **144**, 100 (2009).
12. N. Chakinala, P. R. Gogate and A. G. Chakinala, *Korean J. Chem. Eng.*, **38**, 2468 (2021).
13. Y. Xiao, X.-L. Wang, H. Yu, Y. Yang and X.-t. Dong, *J. Phys. Chem. Solids*, **149**, 109793 (2021).
14. T. K. Vo, W.-S. Kim and J. Kim, *Korean J. Chem. Eng.*, **37**, 1206 (2020).
15. T. K. Vo, D. C. Hau, V. C. Nguyen, D. T. Quang and J. Kim, *Appl. Surf. Sci.*, **546**, 149087 (2021).
16. R. Liang, L. Shen, F. Jing, N. Qin and L. Wu, *ACS Appl. Mater. Interfaces*, **7**, 9507 (2015).
17. S. Hu, M. Liu, K. Li, C. Song, G. Zhang and X. Guo, *RSC Adv.*, **7**, 581 (2017).
18. T.-T. Li, L.-L. Dang, C.-C. Zhao, Z.-Y. Lv, X.-G. Yang, Y. Zhao and S.-H. Zhang, *J. Solid State Chem.*, **304**, 122609 (2021).
19. Y. L. Wang, S. Zhang, Y. F. Zhao, J. Bedia, J. J. Rodriguez and C. Belver, *J. Environ. Chem. Eng.*, **9**, 106087 (2021).
20. H. Wang, X. Yuan, Y. Wu, G. Zeng, H. Dong, X. Chen, L. Leng, Z. Wu and L. Peng, *Appl. Catal. B.*, **186**, 19 (2016).
21. Y. Liu, Y. Zhou, Q. Tang, Q. Li, S. Chen, Z. Sun and H. Wang, *RSC Adv.*, **10**, 1757 (2020).
22. Z. Yang, X. Tong, J. Feng, S. He, M. Fu, X. Niu, T. Zhang, H. Liang, A. Ding and X. Feng, *Chemosphere*, **220**, 98 (2019).
23. X. Zhang, Y. Yang, W. Huang, Y. Yang, Y. Wang, C. He, N. Liu, M. Wu and L. Tang, *Mater. Res. Bull.*, **99**, 349 (2018).
24. P. Zhu, J. Lin, L. Xie, M. Duan, D. Chen, D. Luo and Y. Wu, *Langmuir*, **37**, 13309 (2021).
25. J. Xu, J. Xu, S. Jiang, Y. Cao, K. Xu, Q. Zhang and L. Wang, *Environ. Sci. Pollut. Res.*, **27**, 37839 (2020).
26. A. S. Sindhu, N. B. Shinde, S. Harish, M. Navaneethan and S. K. Eswaran, *Chemosphere*, **287**, 132347 (2022).
27. M. Dinari and F. Dadkhah, *Appl. Organomet. Chem.*, **35**, e6355 (2021).
28. N. Guijarro, P. Bornoz, M. Prévot, X. Yu, X. Zhu, M. Johnson, X. Jeanbourquin, F. Le Formal and K. Sivula, *Sustain. Energy Fuels*, **2**, 103 (2018).
29. X. Yuan, H. Wang, Y. Wu, X. Chen, G. Zeng, L. Leng and C. Zhang, *Catal. Commun.*, **61**, 62 (2015).
30. Y. Shen, Y. Wu, X. Li, Q. Zhao and Y. Hou, *Mater. Lett.*, **96**, 85 (2013).
31. T. K. Vo and J. Kim, *Environ. Sci. Pollut. Res.*, **28**, 68261 (2021).
32. H. Ji, X. Jing, Y. Xu, J. Yan, H. Li, Y. Li, L. Huang, Q. Zhang, H. Xu and H. Li, *RSC Adv.*, **5**, 57960 (2015).
33. T. Zhou, G. Zhang, P. Ma, X. Qiu, H. Zhang, H. Yang and G. Liu, *J. Alloys Compd.*, **735**, 1277 (2018).
34. N. Huo, Y. Yin, W. Liu, J. Zhang, Y. Ding, Q. Wang, Z. Shi and S. Yang, *New J. Chem.*, **40**, 7068 (2016).
35. T. K. Vo, W.-S. Kim and J. Kim, *Korean J. Chem. Eng.*, **37**, 1206 (2020).
36. V. T. Ky and D. T. Quang, *Vietnam J. Chem.*, **59**, 667 (2021).
37. A. Wang, Y. Zhou, Z. Wang, M. Chen, L. Sun and X. Liu, *RSC Adv.*, **6**, 3671 (2016).
38. J. N. Baby, B. Sriram, S.-F. Wang and M. George, *ACS Sustain. Chem. Eng.*, **8**, 1479 (2020).
39. X. T. Cao, T. K. Vo, T. N. M. An, T. D. Nguyen, D. M. Kabtamu and S. Kumar, *ChemistrySelect*, **6**, 4689 (2021).
40. T. K. Vo, V. N. Le, D. T. Quang, M. Song, D. Kim and J. Kim, *Micropor. Mesopor. Mater.*, **306**, 110405 (2020).
41. X. Xu, R. Liu, Y. Cui, X. Liang, C. Lei, S. Meng, Y. Ma, Z. Lei and Z. Yang, *Appl. Catal. B.*, **210**, 484 (2017).
42. X. Lei, X. Li, Z. Ruan, T. Zhang, F. Pan, Q. Li, D. Xia and J. Fu, *J. Mol. Liq.*, **266**, 122 (2018).
43. J. Jiang, W. Fan, X. Zhang, H. Bai, Y. Liu, S. Huang, B. Mao, S. Yuan, C. Liu and W. Shi, *New J. Chem.*, **40**, 538 (2016).
44. P. Garcia-Muñoz, F. Fresno, V. A. de la Peña O'Shea and N. Keller, *Top Curr. Chem.*, **378**, 6 (2019).
45. S. Li, X. Wang, Q. He, Q. Chen, Y. Xu, H. Yang, M. Lü, F. Wei and X. Liu, *Chin. J. Catal.*, **37**, 367 (2016).